Title

Deciphering cryptic methane cycling: Coupling of methylotrophic methanogenesis and anaerobic oxidation of methane in hypersaline coastal wetland sediment

Authors

Krause, Sebastian JE
Treude, Tina

Publication Date

2021-06-01

DOI

10.1016/j.gca.2021.03.021

Peer reviewed

Available online at www.sciencedirect.com

ScienceDirect

Geochimica et Cosmochimica Acta 302 (2021) 160–174

Geochimica et Cosmochimica Acta

www.elsevier.com/locate/gca

Deciphering cryptic methane cycling: Coupling of methylotrophic methanogenesis and anaerobic oxidation of methane in hypersaline coastal wetland sediment

Sebastian J.E. Krause [a], Tina Treude [a,b,*]

[a] Department of Earth, Planetary and Space Sciences, University of California, Los Angeles, Los Angeles, CA 90095, USA
[b] Department of Atmospheric and Oceanic Sciences, University of California, Los Angeles, Los Angeles, CA 90095, USA

Received 9 July 2020; accepted in revised form 22 March 2021; Available online 30 March 2021

Abstract

Methanogenesis has recently been shown to fuel anaerobic oxidation of methane (AOM) within the sulfate-reducing zone of marine sediments, coining the term "cryptic methane cycle". Here we present research on the relationship between methanogenesis and AOM in a shallow hypersaline pool (~130 PSU) within a southern California coastal wetland. Sediment (top 20 cm) was subjected to geochemical analyses, in-vitro slurry experiments, and radiotracer incubations using $^{35}S\text{-}SO_4^{2-}$, ^{14}C-mono-methylamine, and $^{14}C\text{-}CH_4$, to study sulfate reduction, methylotrophic methanogenesis, and AOM. An adapted radioisotope method was used to follow cryptic methane cycling in ^{14}C-mono-methylamine labeling incubations with increasing incubation times (1 hour to three weeks). Results showed peaks in AOM (max 13 nmol cm^{-3} d^{-1}) and sulfate reduction activity (max 728 nmol cm^{-3} d^{-1}) within the top 6 cm. Below 6 cm, AOM activity continued (max 15 nmol cm^{-3} d^{-1}), while sulfate reduction was absent despite 67 mM sulfate, suggesting AOM was coupled to the reduction of iron. Methane concentrations were low (<50 nM) throughout the sediment. Batch sediment slurry incubations with methylated substrates (mono-methylamine and methanol) stimulated methanogenesis, pointing to the presence of methylotrophic methanogens. Incubations with ^{14}C-mono-methylamine revealed the simultaneous activity of methanogenesis and coupled AOM through the stepwise transfer of ^{14}C from mono-methylamine to CO_2 via methane. Our results suggest that AOM is a crucial process in coastal wetland sediments to prevent the buildup of methane in the sulfate-reducing zone. We propose that cryptic methane cycling has been largely overlooked in coastal wetlands resulting in incomplete understanding of carbon cycling in this environment.

Keywords: Sulfate reduction; Iron reduction; Mono-methylamine; Methanol; Salt marsh; Metabolic activity; Radiotracer

1. INTRODUCTION

In the atmosphere, methane is a potent greenhouse gas that traps ~25 times more heat than CO_2 (IPCC, 2014). Atmospheric methane has doubled from 722 ppb in pre-industrial times to ~1850 ppb in 2017 (Nisbet et al., 2019; Saunois et al., 2020) and hence we urgently need to comprehend the mechanisms controlling its emission.

Natural wetlands are the largest contributor of methane into the atmosphere (IPCC, 2007; IPCC, 2014). They fall into two categories: coastal and freshwater. Both environments are characterized by high organic matter loading into sediment, which stimulates microbial methane production (Segers, 1998; Le Mer and Roger, 2001; Reddy and DeLaune, 2008). However, coastal wetlands emit far less methane (1.3 g CH_4 m^{-2} yr^{-1}) into the atmosphere than freshwater wetlands (7.1 g CH_4 m^{-2} yr^{-1}) (Bridgham

* Corresponding author at: Department of Earth, Planetary and Space Sciences, University of California, Los Angeles, Los Angeles, CA 90095, USA.
E-mail address: ttreude@g.ucla.edu (T. Treude).

https://doi.org/10.1016/j.gca.2021.03.021
0016-7037/

et al., 2006, 2013). This discrepancy is due to the connection of coastal wetlands to the ocean, which supplies sulfate to fuel microbial sulfate reduction (SR) and sulfate-dependent anaerobic oxidation of methane (AOM) in anoxic sediments. Both processes suppress major releases of methane into the atmosphere (Segers, 1998; Le Mer and Roger, 2001; Reddy and DeLaune, 2008).

Microbial methanogenesis is the last step in carbon remineralization in water-logged sediments (Stephenson and Stickland, 1933; Thauer, 1998). The process generates methane from the following sources: hydrogen and carbon dioxide (hydrogenotrophic pathway) (Eq. (1)), acetate (acetolactic pathway) (Eq. (2)), and methylated substrates (methanol, methylamines and methylsulfides) (methylotrophic pathway) (Eqs. (3) and (4)).

$$4H_2 + CO_2 \rightarrow CH_4 + 2H_2O \quad (1)$$

$$CH_3COO^- + H^+ \rightarrow CO_2 + CH_4 \quad (2)$$

$$4CH_3OH \rightarrow 3CH_4 + CO_2 + 2H_2O \quad (3)$$

$$4CH_3NH_2 + 2H_2O \rightarrow 3CH_4 + CO_2 + 4NH_4 \quad (4)$$

These pathways are facilitated by anaerobic archaea belonging to the Euryarchaeota Phyla. Hydrogen and acetate are competitive substrates, as they are also metabolized by sulfate-reducing bacteria, which tend to thermodynamically outcompete methanogens and thus suppress the production of methane in the presence of sulfate (Kristjansson et al., 1982; Winfrey and Ward, 1983; Lovley and Klug, 1986; Jørgensen, 2000). Consequently, methane builds up below the penetration depth of sulfate, i.e., in the absence of SR. In the zone where methane and sulfate overlap, methane is consumed by AOM with sulfate as the terminal electron acceptor (Eq. (5)). The process effectively removes roughly 90% of methane before reaching the water column (Hinrichs and Boetius, 2002; Reeburgh, 2007; Knittel and Boetius, 2009). AOM is mediated by a syntrophic consortium of anaerobic methanotrophic archaea (ANME) and sulfate-reducing bacteria (Boetius et al., 2000; Orphan et al., 2001; Michaelis et al., 2002; Knittel and Boetius, 2009).

$$CH_4 + SO_4^{2-} \rightarrow HCO_3^- + HS^- + H_2O \quad (5)$$

While hydrogenotrophic and acetoclastic methanogenesis is largely inhibited in the sulfate-reducing zone, methanogenesis can sustain its activity through methylotrophic pathways. It is well established that methylated compounds (methanol, methylamine, methyl sulfides) are important non-competitive substrates for methanogenesis in sulfate-reducing sediments (Oremland and Polcin, 1982; Lovley and Klug, 1986; Maltby et al., 2016, 2018; Zhuang et al., 2016, 2018). Methanol sources include the degradation of lignin and pectin commonly found in terrestrial plant cell walls (Donnelly and Dagley, 1980; Schink and Zeikus, 1980). Methylamines and methyl sulfides are formed from the degradation of osmolytes such as glycine and betaine, and dimethylsulfoniopropinate, which are particularly abundant in saline and hypersaline environments (Oren, 1990; Zhuang et al., 2011, 2016). Methylotrophic methanogenesis has been detected in organic-rich, sulfate-reducing sediments of various aquatic environments such as intertidal estuaries and salt marshes (Oremland et al., 1982), river deltas (Zhuang et al., 2018), upwelling regions (Maltby et al., 2016), and eutrophic shelf sediments (Maltby et al., 2018).

Despite strong evidences for methylotrophic methanogenesis in the sulfate-reducing zone, methane concentrations are considerably lower than in the deeper sulfate-free zone (Iversen and Jørgensen, 1985; Treude et al., 2005a, 2005b; Jørgensen and Kasten, 2006). Current research on the activity of methanogens in the sulfate-reducing zone of organic-rich sediments stimulated some speculation on the whereabouts of the produced methane and whether it could directly feed into AOM (Maltby et al., 2016; Maltby et al., 2018; Zhuang et al., 2019). Two recent studies using a combination of ^{13}C-CH_4 labeling and isotope dilution modeling provided the first evidence for a simultaneous production and consumption of methane and coined the 'cryptic methane cycle' (Xiao et al., 2017; Xiao et al., 2018). Experiments were conducted with anoxic organic-rich coastal sediments, which were spiked with ^{13}C-CH_4. The development of the ^{13}C-CH_4 signal was followed over time. The applied model presumed that the mole fraction of ^{13}C-CH_4 (^{13}C-CH_4 /(^{13}C-CH_4 + ^{12}C-CH_4)) changes through time as a result of production of methane from indigenous sources and consumption of methane due to AOM in the sediment. Community profiling revealed the presence of both hydrogenotrophic and methylotrophic methanogens among the methanogenic archaea, while incubations with ^{14}C-labeled methanogenic substrates identified methylotrophic methanogenesis as the major pathway of methane production in the sediment.

Although it appears that AOM is the key to regulating methane in the sulfate-reducing zone, there are virtually no studies on the fate of methane produced from non-competitive methylotrophic methanogenesis in this environment. Notably, if AOM is active in the same zone as methanogenesis, the buildup and eventual emission of methane would be hampered, if not prevented. It would explain, why only low levels of methane are detected in the sulfate-reducing zone, notwithstanding the presence of methanogenesis. Additionally, confirmation of a rapid turnover of methane in this zone would suggest that past gross methane budgets from wetlands were underestimated. Detection and quantification of this cryptic methane cycle is therefore essential to complement our understanding of carbon cycling in coastal wetlands.

With the application of an adapted radiotracer technique, this work will demonstrate the passage of carbon from a methylated substrate via methane to inorganic carbon within the sulfate-reducing zone of a coastal wetland. Our method shows that the methane source (i.e., methylotrophic methanogenesis) is spatially directly linked to its sink (AOM), hampering the buildup of methane in the sediment. This proof of concept study will provide an important step forward for the investigation of methane-related carbon cycling in coastal wetland sediments.

2. METHODS

2.1. Study area and field sampling

The Carpinteria Salt Marsh Reserve (CSMR) is part of the University of California Natural Reserve System spanning a total of 230 acres of which 120 belong to the Natural Reserve System (Fig. 1A). Three major creeks run through and converge within the CSMR, and empty into the Pacific Ocean at its most southern end (Page et al., 1995). We selected a hypersaline pool within the CSMR (34°23′56.1″N 119°32′10.2″W) that exhibited black sulfidic sediments, indicative of a sulfate-reducing environment, and very little evidence of bioturbation, suggesting that sediments were largely anoxic (Fig. 1B and C). During the sampling period, the pool had no visible supply of water from creeks, streams, or the ocean. However, salt crusts visible around the pool (Fig. 1B) and high salinity of the pool water (132 PSU, Fig. 2A) pointed towards past ocean influence.

Sediment cores were collected in June 2018. The top ~20 cm of sediment was sampled by hand using large (10 cm i.d.) and small (2.6 cm i.d.) polycarbonate push core liners. Sediments were characterized by a brown surface (~0–1 cm), a distinct black (~1–8 cm) and grey/brown (>8 cm) layer. Water depth above the sampled sediment was approximately 10 cm. Liners were spaced at ~20 cm distance to facilitate sufficient space for extraction and closeness for comparability. Extraction of the sediment core was accomplished by careful removal of sediment around the liner and then placing a metal plate under the bottom of the liner for safe lifting. The air headspace remaining in the liner was carefully filled with water from the hypersaline pool and sealed bubble-free with rubber stoppers and electrical tape, to minimize disturbance of the surface sediment during transport. After same-day arrival at the home laboratory, all sediment cores were stored at 4 °C, in the dark, and processed within 1 d to 3 months of collection, depending on the type of analyses (for more details see below).

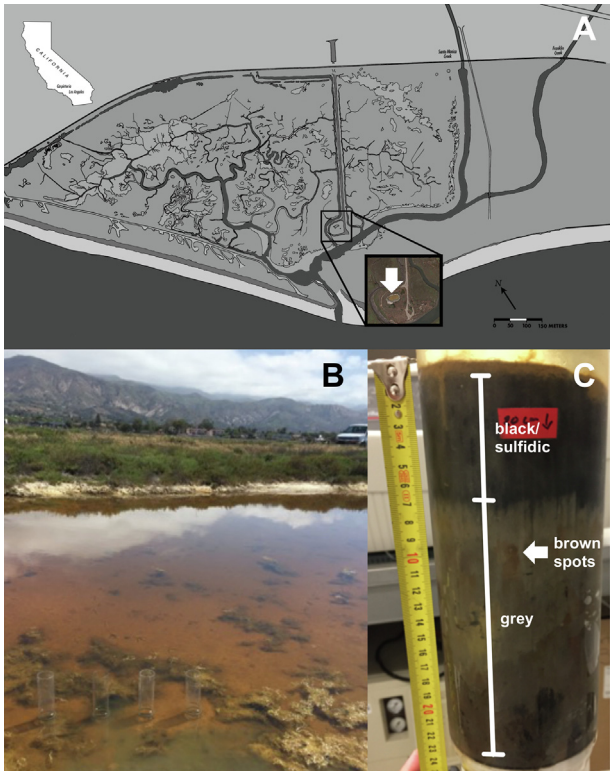

Fig. 1. Study Site: (A) Map of the Carpinteria Salt Marsh Reserve and location of the hypersaline pool (white arrow); map courtesy of A. Brooks; inserted satellite image from Google Maps. (B) Hypersaline pool with large push core liners placed for sampling. (C) Side view of a large sediment push core used for porewater extraction. Coloration of the sediment is labeled. For more details see text.

2.2. Porewater geochemistry

For analyses of sediment porewater geochemistry, one large sediment push core was subsampled 1 d after collection. The core was sliced under a constant flow of argon to minimize oxidation of oxygen-sensitive solutes. The top sampled sediment layer, which had a high-water content, had a thickness of 1.5 cm. Below 1.5 cm, sediments were sliced evenly in 1 cm increments. All sediment layers were transferred into argon-flushed 50 mL conical centrifuge tubes and centrifuged at 4300*g* for 20 min to separate porewater from sediment. Porewater was immediately analyzed for dissolved sulfide according to Cline (1969) and iron (II) according to Grasshoff et al. (1999). Concentrations of the solutes were determined with a Shimadzu UV-Spectrophotometer (UV-1800). Remaining porewater was collected in plastic vials, stored at 4 °C, and later analyzed for sulfate and chloride concentrations using an ion chromatograph (Metrohm 761) according to Dale et al. (2015). Salinity in the porewater was calculated from chlorinity using Knudsen's equation (Knudsen, 1901). Porosity of the sediment was determined by calculating the difference between sediment wet and dry weight divided by its volume. Sediment density was determined by dividing wet weight of the sediment by its volume.

2.3. In-vitro methanogenesis

Two months after sample collection, one large push core was sliced into two layers (0–8 and 8–16 cm), distinguished by distinct black (1–8 cm) and grey/brown (8–16 cm) coloring, to study *in-vitro* methanogenesis after the addition of different substrates and inhibitors. Each layer was quickly subsampled using 3 mL cut-off plastic syringes under a steady flow of argon to minimize oxygen exposure. Ten mL of sediment were transferred into sterilized, argon-flushed 60 mL glass serum vials, sealed with blue butyl rubber stoppers (Bellco Glass Inc, 20 mm diameter) and crimped with aluminum crimps. Ten mL of artificial seawater medium, prepared according to Widdel and Bak (1992) and adjusted to sediment porewater salinity, was added to the sediments through the rubber stopper to make a 1:1 sediment/medium slurry. Medium was added to all sediment samples except a group of triplicates from each layer, which

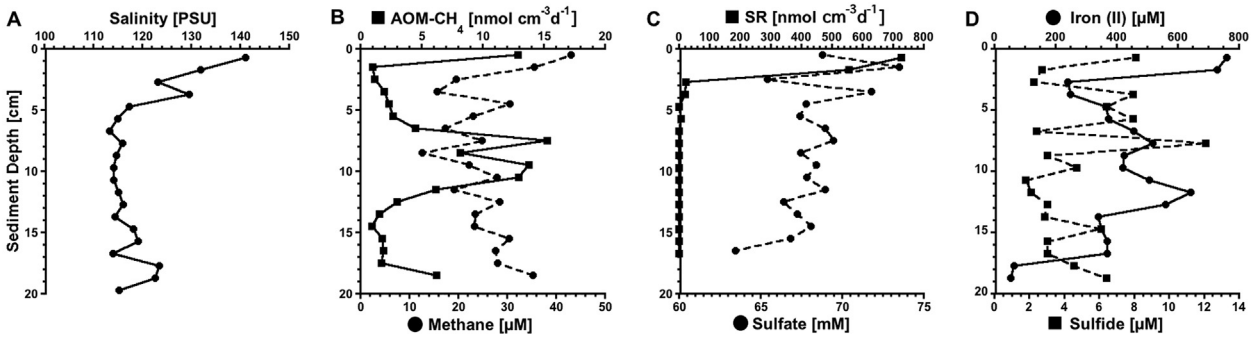

Fig. 2. Depth profiles of biogeochemical parameters in sediment from the hypersaline pool in the CSMR: (A) salinity, (B) methane (determined in the AOM vial) and AOM-CH_4 (determined from the direct injection of ^{14}C-CH_4), (C) porewater sulfate and sulfate reduction (SR), (D) porewater sulfide and iron (II).

served as natural controls (see details below). Finally, the headspace of the sealed serum vials was flushed with argon for one minute to ensure anoxic conditions.

A total of 5 slurry amendments, each in triplicates per sediment layer, were prepared with: (1) 20 mM mono-methylamine (MMA), (2) 20 mM methanol, (3) 30 mM, sodium molybdate, (4) 60 mM, 2-bromoethanosulfonate (BES), (5) no addition (slurry control). In addition, triplicate vials per sediment layer containing undiluted sediment served as natural controls (6). Amendments (1) and (2) served to study methane production from non-competitive methylated substrates. Amendments (3) and (4) served to evaluate methane production in the presence of a sulfate reducer (Oremland and Capone, 1988) and methanogen inhibitor (Hoehler et al., 1994), respectively. Controls (5) and (6) served to study the natural production of methane in diluted and undiluted sediment, respectively. Methane development in the headspace of the vials was monitored for a total of 3700 h.

Methane development in the headspace of the serum vials was tracked using a Shimadzu Gas Chromatograph (GC-2014) with a packed Haysep-D column and a flame ionization detector. The column temperature was 80 °C with helium as the carrier gas at 12 mL per min. Methane concentrations were calibrated against methane standards (Scotty Analyzed Gases) with a ±5% precision.

2.4. Sulfate reduction

SR rates were determined by injecting radioactive, carrier-free ^{35}S-sulfate (^{35}S-SO_4^{2-}; dissolved in MilliQ water, injection volume 10 µL, activity 260 KBq, specific activity 1.59 TBq mg^{-1}) into a small whole-round push core at 1-cm increments according to Jørgensen (1978). The radiotracer incubation started one month after core collection. Twenty-four hours prior to the injection of ^{35}S-SO_4^{2-}, the core was transferred from 4 °C storage to room temperature (in the dark). Radiotracer incubation was terminated after 24 h by slicing the cores in 1-cm increments into 50 mL centrifuge tubes filled with 20 mL 20% (w/w) zinc acetate solution. Each sample vial was shaken thoroughly to stop biological activity in the sediment and stored at −30 °C until analyses. Control samples were prepared by slicing sediment from an additional small push core in 1-cm increments into tubes with zinc acetate before radiotracer addition. Samples were analyzed and rates calculated according to the cold-chromium distillation method (Kallmeyer et al., 2004).

2.5. Methanogenesis and AOM from ^{14}C-MMA

The main goal of this study was to follow (within the sulfate-rich zone) the conversion of a non-competitive substrate to methane by methanogenesis (MG-MMA), and the subsequent conversion of the produced methane to inorganic carbon by AOM (AOM-MMA). Tracking both processes simultaneously was accomplished by injecting whole round sediment cores with ^{14}C-labeled mono-methylamine (^{14}C-MMA) as representative methylated methanogen substrate. The concept of this method is that methanogens convert ^{14}C-MMA to ^{14}C-methane (^{14}C-CH_4), which is then converted to ^{14}C-total inorganic carbon (^{14}C-TIC) via AOM. In the presence of both processes, we expect to find all three ^{14}C-compounds in the same sample after the incubation. With increasing incubation time, ^{14}C should move cumulatively from ^{14}C-MMA (via ^{14}C-CH_4) to ^{14}C-TIC. If AOM effectively removes methane at the rate of production, we expect to find no significant accumulation of ^{14}C-CH_4 in the sediment.

Twenty-four hours before sediment was injected with ^{14}C-MMA, six small sediment push cores were transferred to room temperature (in the dark) after storage for one month at 4 °C. Four of the push cores were injected with ^{14}C-MMA (^{14}C-mono-methylamine; dissolved in 1 mL water, injection volume 10 µL, activity 220 KBq, specific activity 1.85–2.22 GBq $mmol^{-1}$) and incubated for 1 h, 1 d, 1 wk and 3 wk, respectively, at room temperature, in the dark, to follow the step-wise conversion of ^{14}C-MMA via ^{14}C-CH_4 to ^{14}C-TIC. The incubations were terminated by slicing the cores at 1-cm increments into 50 mL wide-mouth crimp glass vials filled with 20 mL of 2.5% NaOH. Vials were sealed with butyl stoppers and aluminum crimps immediately and shaken thoroughly to stop biological activity in the sediment and to separate ^{14}C-CH4 in the headspace from ^{14}C-MMA and ^{14}C-TIC in the liquid/solid phase of the sample. The 5th small push core was desig-

nated as the ^{14}C-MMA control core. The control core was sliced at 1-cm increments into vials with NaOH prior to radiotracer addition. Processing of the 6th core will be described under Section 2.5.3.

2.5.1. Determination of total CH_4 and ^{14}C-CH_4

Prior to the analyses of ^{14}C-CH_4 in the sample headspace, total CH_4 was determined by gas chromatography (Shimadzu GC-2014, see Section 2.3) from a small headspace sub-sample (100 µl). Analysis of ^{14}C-CH_4 was accomplished using a modified method by Treude et al. (2005a), which was combined with a series of cold traps adapted from Zhuang et al. (2017) to prevent potential contaminations with volatile ^{14}C-MMA or ^{14}C-CO_2. The full analytical setup is displayed in Fig. 3. In this adapted procedure, the headspace of the vial was purged with compressed air through a combustion oven (850 °C) with copper (II) oxide to combust microbially produced ^{14}C-CH_4 to ^{14}C-CO_2. Additional traps were placed in line as follows, to prevent potential contaminations with other ^{14}C compounds: Impurities of volatilized ^{14}C-MMA were separated by passing the sample headspace through a 15 mL glass Hungate tube containing 10 mL of cold (0 °C) 0.1 M citric acid buffer solution (19.3 g citric acid + 4 g NaOH per liter of water, pH 4). Impurities of volatilized ^{14}C-CO_2 were separated by passing the gas headspace through a consecutive 15 mL Hungate tube, containing 10 mL of cold (0 °C) 5% (w/w) sodium hydroxide. Both traps were held in a pre-frozen cryo safe cooler (Bel-Art, Junior 0 °C). The purified headspace, containing CH_4 as the only ^{14}C-labelled compound, was then passed through a quartz column filled with granular copper (II) oxide placed in a combustion oven (850 °C) to oxidize ^{14}C-CH_4 to ^{14}C-CO_2. After exiting the oven, the headspace with ^{14}C-CO_2 was then passed through a 20 mL scintillation vial containing 10 mL of citric acid buffer (pH 4, room temperature) to capture any water vapor, which could condense to tubing walls and collect ^{14}C-CO_2. Finally, the ^{14}C-CO_2 of the headspace was collected in two consecutive 20 mL scintillation vials filled with 10 mL of phenylethylamine and metoxyethanol (1:7 mixture, at room temperature). Oven timeseries tests conducted prior to sample analysis showed that > 99% of ^{14}C-CH_4 is combusted to ^{14}C-CO_2 and collected in the CO_2 capture vials after 20 min of headspace flushing. Radioactivity in both scintillation vials was determined by liquid scintillation counting after adding 10 ml scintillation cocktail (Ultima Gold XR, Perkin Elmer).

Prior to analyzing the first samples, the efficiency of all cold traps to capture ^{14}C-impurities was tested. Test samples were prepared by filling sample vials with 25 ml 5% NaOH to replicate the total volume of a sample containing sodium hydroxide (20 mL) and sediment (~5 mL). Added to the samples vials was either ^{14}C-MMA, ^{14}C-CH_4, ^{14}C-TIC (the latter in the form of ^{14}C-bicarbonate). Test samples were sealed and run through the combustion setup (see Section 2). Activity of all impurity traps and the final traps that captured the combusted ^{14}C-CH_4 was determined by liquid scintillation counting. Test samples with added ^{14}C-CH_4 showed that 97–99% of the analyzed ^{14}C was detected in the final methoxyethanol/phenylethylamine traps (CO_2 traps) (Fig. 3, #11). The remaining 1–3% of the ^{14}C was detected in the citric acid trap (Fig. 3, #10).

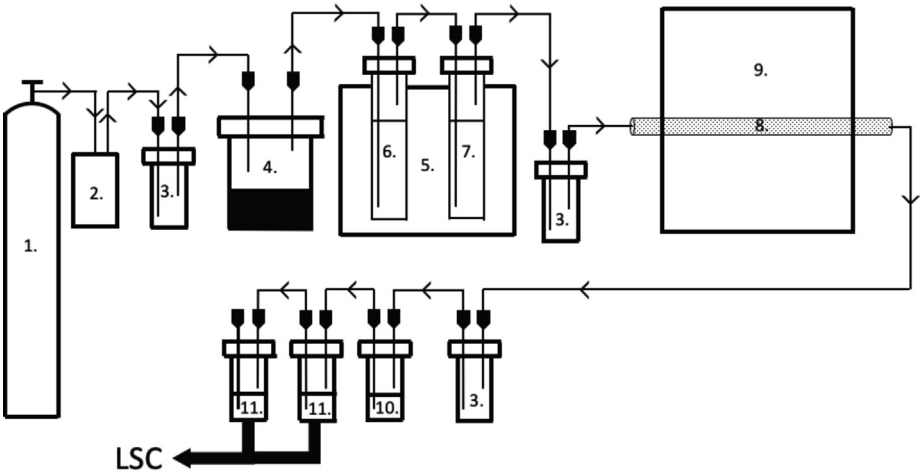

Fig. 3. Schematic of the method used to purge, combust, and trap ^{14}C-CH_4 from the sample vial headspace, while removing all potential volatile ^{14}C impurities (^{14}C-MMA and ^{14}C-CO_2) via intermediate traps. Narrow arrows indicate the direction of the gas flow. Labels: (1) compressed air tank, (2) mass flow controller (Analyt MTC), (3) safety vial: empty glass crimp vial (10 ml), (4) sample vial: glass crimp vial (50 ml) with sample and headspace, (5) cryo box, 0 °C (Bel Art), (6) ^{14}C-MMA trap: Hungate tube (15 ml) filled with citric acid buffer (10 ml, pH 4, 0 °C), (7) ^{14}C-CO_2 trap: Hungate tube filled with 5% w/w NaOH (10 ml, pH 14, 0 °C), (8) quartz column with granular copper (II) oxide, (9) combustion oven (850 °C), (10) H_2O trap: glass crimp vial (10 ml) filled with citric acid buffer (10 ml, pH 4), (11) $^{14}CO_2$-trap (for combusted ^{14}C-CH_4): two consecutive scintillation vials (20 ml) filled with 10 ml phenylethylamine/methoxyethanol (1:7 mixture), (LSC) liquid scintillation counting. Tubing (in direction of flow): copper (between tank and controller), TYGON (between controller and the second safety trap), ISO-VERSINIC (before/after oven), TYGON (between the third safety trap and the second scintillation vial). Gas enters/exists vials from/into tubing via luer connectors/needles. Note that objects are not to scale. The method was adapted from Treude et al. (2005a) and Zhuang et al. (2017). For more details see text.

Oven test samples with added ^{14}C-MMA showed that 99.97% of the ^{14}C remained in the sample vial, while <0.01% was detected in the cold citric acid (Fig. 3, #6), <0.01% in the cold NaOH cold trap (Fig. 3, #7) and <0.01% in the CO_2 traps (Fig. 3, #11). Oven test samples with added ^{14}C-TIC (in the form of ^{14}C-bicarbonate) showed that 99.97% of the ^{14}C remained in the sample vial, while < 0.01% was detected in the cold citric acid (Fig. 3, #6), <0.01% in the cold NaOH cold trap (Fig. 3, #7) and < 0.01% in the CO_2 traps (Fig. 3, #11).

2.5.2. Determination of ^{14}C-MMA and ^{14}C-TIC

Total ^{14}C activity in the liquid sample (i.e., the sum of residual ^{14}C-MMA and the dissolved fraction of the produced ^{14}C-TIC) was determined by subsampling 100 µL of clear supernatant from the sample vial into a 6 ml scintillation vial, to which 1 mL ultrapure water and 3 mL scintillation cocktail (Ultima Gold XR, Perkin Elmer) was added before liquid scintillation counting. Note that this procedure does not capture potential ^{14}C-$CaCO_3$ precipitates in the solid phase of the sample. Any ^{14}C that was present in the solid phase as ^{14}C-$CaCO_3$ would lead to an overestimation of the rates, because it would underestimate the pool of ^{14}C injected at the start of the incubation. However, since microbially-induced carbonate precipitations can be expected to be a sluggish process even under optimized conditions (Krause, 2012), we expect no significant overestimation of rates for the applied incubation times.

The total produced ^{14}C-TIC (including potential ^{14}C-$CaCO_3$ precipitates) was determined by acidification according to Joye et al. (2004). The sample vial was opened and weighed before and after the sample was transferred to a 250 mL Erlenmeyer flask to determine the sample weight. After transfer to the Erlenmeyer flask, a drop of antifoam agent (Antifoam B Silicon Emulsion) was added to prevent excessive foaming after acidification. The Erlenmeyer flask was then sealed with a butyl stopper, which was prepped with a metal wire threaded through the stopper and a plastic ring at the end of the wire. The ring was used to hold an open 6 mL scintillation vial filled with a mixture of 1 mL of phenylethylamine and 1 mL of 2.5% (w/w) NaOH, which served as a trap for ^{14}C-CO_2. The sample was acidified by injecting 6 mL of 6 M hydrochloric acid using a 10 mL syringe equipped with a long needle. The needle of the loaded syringe was held in place between the butyl stopper and the glass of the Erlenmeyer flask while acid was injected. After injection, the needle was removed quickly, and the stopper was fixed with a metal clip. The Erlenmeyer flask was then placed on a shaking table for 4 h to ensure all ^{14}C-TIC was converted to ^{14}C-CO_2, released into the headspace, and captured in the ^{14}C-CO_2 trap. The scintillation vial was then removed from the flask and radioactivity was determined by liquid scintillation (see above). The resulting value, which represents the total ^{14}C-TIC, was then subtracted from the total ^{14}C activity in the liquid sample (see above) to determine the activity of the residual ^{14}C-MMA in the liquid phase.

Prior to sample analysis, test samples containing only NaOH solution and ^{14}C-MMA were sent through the same procedure to test if ^{14}C-MMA is accidently captured by the suspended ^{14}C-CO_2 trap. These samples showed that 99.99% of the ^{14}C remained in the NaOH supernatant and <0.01% was detected in the CO_2 trap. Vice versa, test samples containing only NaOH and ^{14}C-TIC (in the form of ^{14}C-bicarbonate) showed that 99.99% of the ^{14}C was captured in the CO_2 trap while <0.01% of the ^{14}C remained in the NaOH supernatant after acidification/shaking.

2.5.3. Determination of ^{14}C-MMA recovery from sediment

Methylated amines bind to sediment surfaces and therefore quantification of methylated amines from sediment porewaters underestimates the total amount present in the sediment (Wang and Lee, 1993, 1994; Xiao and Peacock, 2019). The recovery factor of ^{14}C-MMA from sediment was determined as follows: the top 5 cm of the 6th small push core from the hypersaline pool was sliced at 1-cm intervals, and each sediment slice was transferred to 250 ml Erlenmeyer flasks with NaOH similar to the above procedure (Section 2.5.2) to produce a total of 5 killed sediment samples. An additional set of three 250 ml Erlenmeyer flasks containing only NaOH (no sediment) served for the determination of the total added ^{14}C-MMA. A magnetic stir bar was added to each Erlenmeyer flask, and each flask was placed on a magnetic stir plate. After the sediment was homogeneously mixed with the NaOH, ^{14}C-MMA (dissolved in water, 1 mL, 220 kBq, 1.85–2.22 GBq specific activity) was added to each flask (killed samples and NaOH samples) and stirred into the samples. The two setups were then shaken for 4 h. After shaking and resting, 100 µl of the clear supernatant was subsampled from all flasks, and radioactivity was determined by liquid scintillation (see Section 2). The recovery factor was calculated as follows (Eq. (6)):

$$\mathrm{RF} = [\frac{a_{SED}}{a_{NaOH}}] \quad (6)$$

where RF is the recovery factor; a_{SED} is the averaged amount of radioactivity (CPM) recovered from the flasks containing NaOH and the sediment sample; a_{NaOH} is the averaged amount of radioactivity (CPM) recovered from the flasks containing only NaOH. The total amount of ^{14}C-MMA in samples was then determined by dividing the ^{14}C-MMA determined in Section 2.5.2 by the recovery factor (see Eq. (7)).

The tested sediment samples showed a mean ^{14}C-MMA recovery of 46% after shaking and acidification compared to sediment-free controls. The standard deviation of CPM recovered from five test samples was 22.5%, while the standard deviation of CPM recovered from three controls was 3%. The determined recovery factor (0.46, Eq. (6)) was applied to calculate the total CPM of ^{14}C-MMA.

2.5.4. Calculations of methanogenesis and AOM rates

Results from ^{14}C-MMA incubations were used to calculate metabolic rate of MG-MMA and coupled AOM-MMA. MG-MMA rate calculations take into consideration the natural porewater concentrations of MMA, residual ^{14}C-MMA, ^{14}C-CH_4, and ^{14}C-TIC (Eq. (7)). The sum of all three ^{14}C-components represents the total amount of ^{14}C-MMA injected at t_0, while the sum of

^{14}C-CH_4 and ^{14}C-TIC represents the metabolic product of methanogenesis at the end of the incubation, assuming that ^{14}C-TIC was derived from ^{14}C-CH_4 after consumption by AOM. Natural concentrations of MMA could not be determined for this study. Fitzsimons et al. (1997) reported MMA concentrations from salt marsh sediment pore water between 0–319 μM. Based on this knowledge, a high (100 μM) and a low (10 μM) MMA concentration was assumed to complete the rate calculations as follows (Eq. (7)):

$$\text{MG-MMA} = \frac{a_{CH_4} + a_{TIC}}{a_{CH_4} + a_{TIC} + \left[\frac{a_{MMA}}{RF}\right]} * \ [MMA]_{LIT} * \frac{1}{t} \qquad (7)$$

where *MG-MMA* is the rate of methanogenesis from MMA (nmol cm^{-3} d^{-1}); a_{CH4} is the produced radioactive methane (CPM); a_{TIC} is the ^{14}C-TIC produced from methane (CPM); a_{MMA} the residual ^{14}C-MMA (CPM); RF is the recovery factor (Eq. (6)); $[MMA]_{LIT}$ is the assumed MMA porewater concentrations from Fitzsimons et al. (1997) (nmol cm^{-3}); t is the incubation time (d). ^{14}C-CH_4 and ^{14}C-TIC sample activity was corrected by respective non-biological activity determined in controls.

Calculation of AOM-MMA rates based on methane produced from ^{14}C-MMA take into consideration the total methane measured from the headspace of the sample vial, ^{14}C-CH_4 produced by MG-MMA, and ^{14}C-TIC produced by AOM (Eq. (8)). The sum of ^{14}C-CH_4 and ^{14}C-TIC represents the total amount of ^{14}C-CH_4 that was produced and available for AOM over the entire incubation, while ^{14}C-TIC represents the metabolic product of AOM at the end of the incubation. Note that concentrations of total methane should usually be taken at the start of an incubation (not at the end as done here). But since methane concentrations remained stable in controls of long-term incubations over the first weeks (see Section 3.2), we felt comfortable using the end concentrations for our calculations. It should be further highlighted that ^{14}C-labeled methane available for AOM was not present at t_0 but instead was produced over time. Hence, AOM rates based on ^{14}C-CH_4 from ^{14}C-MMA represent an underestimation of the actual rate in this approach. AOM-MMA rates were calculated according to Eq. (8):

$$AOM - MMA = \frac{a_{TIC}}{a_{CH_4} + a_{TIC}} * [CH_4] * \frac{1}{t} \qquad (8)$$

where *AOM-MMA* is the AOM rate based on methane produced from MMA (nmol cm^{-3} d^{-1}); a_{TIC} is the produced ^{14}C-TIC (CPM); a_{CH4} is the residual radioactive methane (CPM); $[CH_4]$ is the methane concentration in the sample vial headspace (nmol cm^{-3}); t is the incubation time (d). ^{14}C-TIC activity was corrected by non-biological activity determined in controls.

2.6. AOM from ^{14}C-CH_4

AOM rates determined directly from ^{14}C-CH_4 (AOM-CH_4) were produced by injecting ^{14}C-CH_4 (^{14}C-CH_4 dissolved in anoxic MilliQ, injection volume 15 μL, activity 5 KBq, specific activity 1.85–2.22 GBq $mmol^{-1}$) into a small push core from the hypersaline pool at 1-cm increments similar to the injections procedures in 2.4 and 2.5. One month after storage at 4 °C, and 24 h prior to radiotracer injection, the core was transferred to room temperature (in the dark). After radiotracer injection, the core was incubated for 24 h at room temperature, in the dark. The incubation was terminated by slicing the core at 1-cm increments into 50 mL wide-mouth crimp glass vials filled with 20 mL of 2.5% NaOH. Vials were sealed with butyl stoppers and aluminum crimps immediately and shaken thoroughly to stop biological activity in the sediment. Control samples were prepared by slicing sediment from a separate small pushcore into vials with NaOH before tracer addition. Prior to ^{14}C analysis, total CH_4 concentrations within each vial was determined by extracting a 100 μL gas sample from the headspace of the AOM-CH_4 samples and analyzing it by gas chromatography (see Section 2.5). Residual ^{14}C-CH_4 in the headspace was determined by liquid scintillation counting after combustion to ^{14}C-CO_2 and CO_2-capturing. ^{14}C-TIC produced as a result of AOM was determined by liquid scintillation counting after acidification and shaking. AOM-CH_4 rates were calculated according to Eq. (8).

3. RESULTS

3.1. Biogeochemical characterization of the study site

Porewater salinity in the sediment core (0–20 cm) ranged between ~110–140 PSU characterizing the pool as hypersaline (Fig. 2A). Porewater sulfate concentrations (60–75 mM) were about three times above open ocean seawater concentrations and illustrated that samples were taken within the sulfate-rich zone (Fig. 2C). The highest sulfate concentration (74 mM) was measured at 1.5–2.5 cm. Sulfate gradually decreased with sediment depth displaying the lowest concentration (63 mM) at 16.5–17.5 cm. Microbial SR activity was only detected in the top 6 cm, showing a maximum rate of 728 nmol cm^{-3} d^{-1} at 0–1 cm. Below 6 cm, SR was not detectable despite high concentration of sulfate throughout the core. Porewater sulfide concentrations varied throughout the sediment column (1–12 μM) with one maximum at 7.5–8.5 cm (12 μM) (Fig. 2D). Dissolved iron (II) was detected throughout the sediment column, reaching two maxima (~760 and 642 μM) between 0–2.5 cm and at 11.5–12.5 cm, respectively (Fig. 2D).

Methane concentration determined in the AOM vials peaked (43 nmol cm^{-3}) at 0–1 cm (Fig. 2B). Between 1 and 4 cm, methane decreased to 16 nmol cm^{-3} before increasing again to 30 nmol cm^{-3} at 4–5 cm. Between 5 and 19 cm, methane concentrations varied between 13 and 35 nmol cm^{-3}. AOM activity determined from ^{14}C-CH_4 (AOM-CH_4) was detected within and below the sulfate-reducing zone. Within the sulfate-reducing zone (0–6 cm), a peak in AOM (13 nmol cm^{-3} d^{-1}) was detected at 0–1 cm, which aligned with the highest SR rates and a peak in methane. Below 1 cm, AOM declined along with SR and methane. Below the sulfate-reducing zone, AOM gradually increased again, reaching a broad second peak (4.5 to 15 nmol cm^{-3} d^{-1}) between 6 and 12 cm. These

maxima roughly coincided with elevated iron (II) concentrations (Fig. 2D). Below 12 cm, AOM and iron (II) decreased with depth whereas methane concentrations varied between 22 and 36 nmol cm^{-3} through the rest of the core (Fig. 2B). An additional smaller AOM peak (6 nmol cm^{-3} d^{-1}) was detected at the bottom of the core.

3.2. Response of methanogenesis to different additives

Fig. 4 shows results from the *in-vitro* time-series study of methanogenesis with sediment slurries from the 0–8 cm and 8–16 cm layers. Slurries contained either non-competitive methanogenesis substrates (MMA or MetOH), inhibitors of methanogenesis and SR (BES or molybdate, respectively), or no additives (slurry control). Undiluted sediment without additions served as natural controls.

Methane in the natural control increased only slightly from ca. 40 to 150 ppmv in both the 0–8 cm and 8–16 cm layers over 3700 h (Fig. 4F). The slurry control followed a similar trend (Fig. 4C). Different to the controls, all treatments with non-competitive methanogen substrates showed a steep increase in methane to >40,000 ppmv after 320 h and reached a stationary phase starting at 420 h (Fig. 4A and D). Starting at 1000 h, a slight decrease in methane was observed. Sediments from the bottom 8–16 cm developed slightly higher methane maxima (49,000 and 49,500 ppmv) with MMA and methanol, respectively.

Methane in sediment slurries amended with BES varied without trend between 30 and 60 ppmv in both sediment layers, which was lower than the controls (Fig. 4E). Methane in sediment slurries from 0 to 8 cm amended with molybdate increased from 130 to 1340 ppmv after 400 h and remained between 1260 and 1950 ppmv for the remaining 3400 h (Fig. 4B). One replicate from the top 0–8 cm increased to 7284 ppmv at the end of the incubation. Molybdate-amended slurries from 8 to 16 cm (Fig. 4B) released methane an order of magnitude lower than the respective slurries from 0-8 cm, which was closer to trends found in the slurry controls (Fig. 4C).

3.3. Coupled methanogenesis and AOM

3.3.1. ^{14}C-MMA time-series incubation with sediment cores

Methylotrophic methanogenesis supporting AOM (AOM-MMA) in the sulfate-rich zone was determined by ^{14}C-MMA injections into 4 separate push cores, which were incubated for 1 h, 1 d, 1 wk, and 3 wk, respectively. Fig. 5 shows the radioactivity distribution (percentage of the sum of all ^{14}C in counts per minute = % CPM) between the residual ^{14}C-MMA, the produced ^{14}C-CH_4, and the produced ^{14}C-TIC for the four incubations.

After the 1-h incubation, the majority of radioactivity remained in the residual ^{14}C-MMA (96–99%) throughout

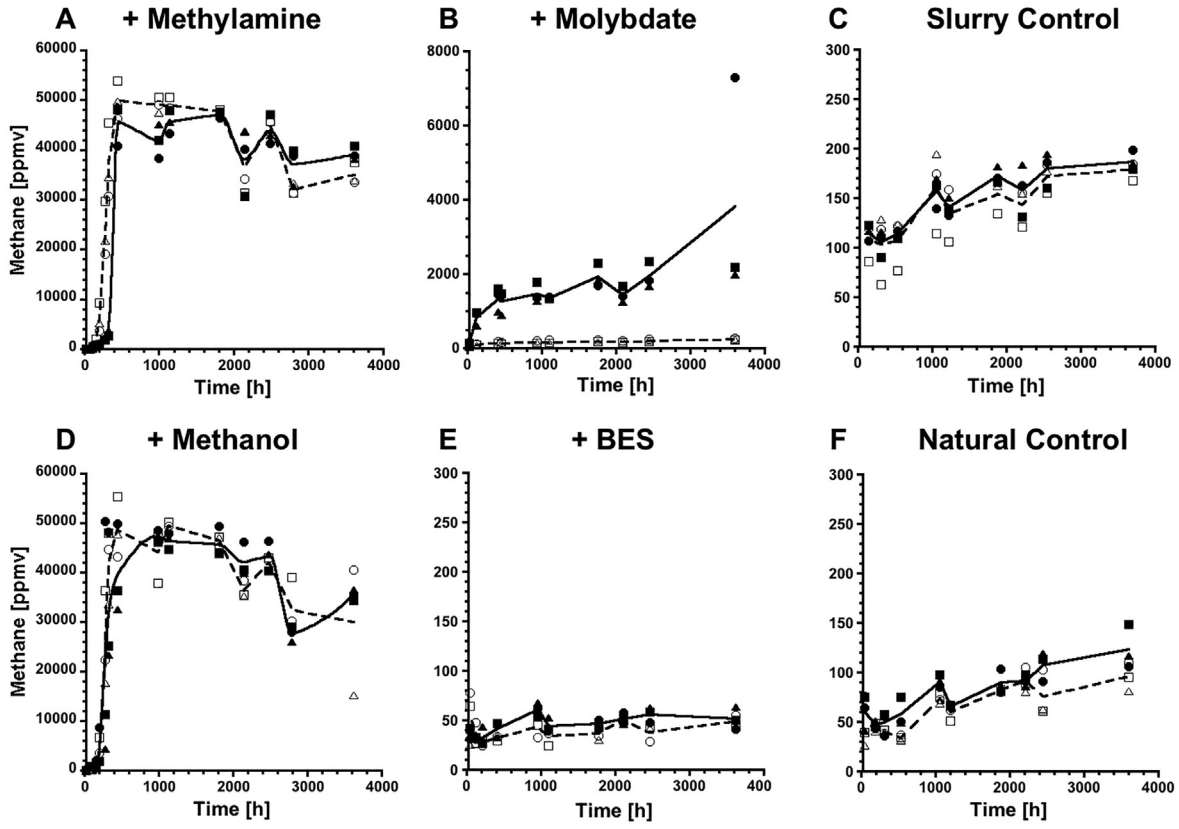

Fig. 4. Temporal development of methane (ppmv) in the headspace of incubation vials containing sediment slurries from the 0–8 cm (solid line and filled symbols) and 8–16 cm (dashed line and open symbols) layer of the hypersaline pool. Slurries were treated with monomethylamine (20 mM, A), methanol (20 mM, D), molybdate (30 mM, B), BES (60 mM, E). Slurries without additives (slurry control, C) and undiluted sediment (natural control, F) served as controls. Note the different scales on the y-axes.

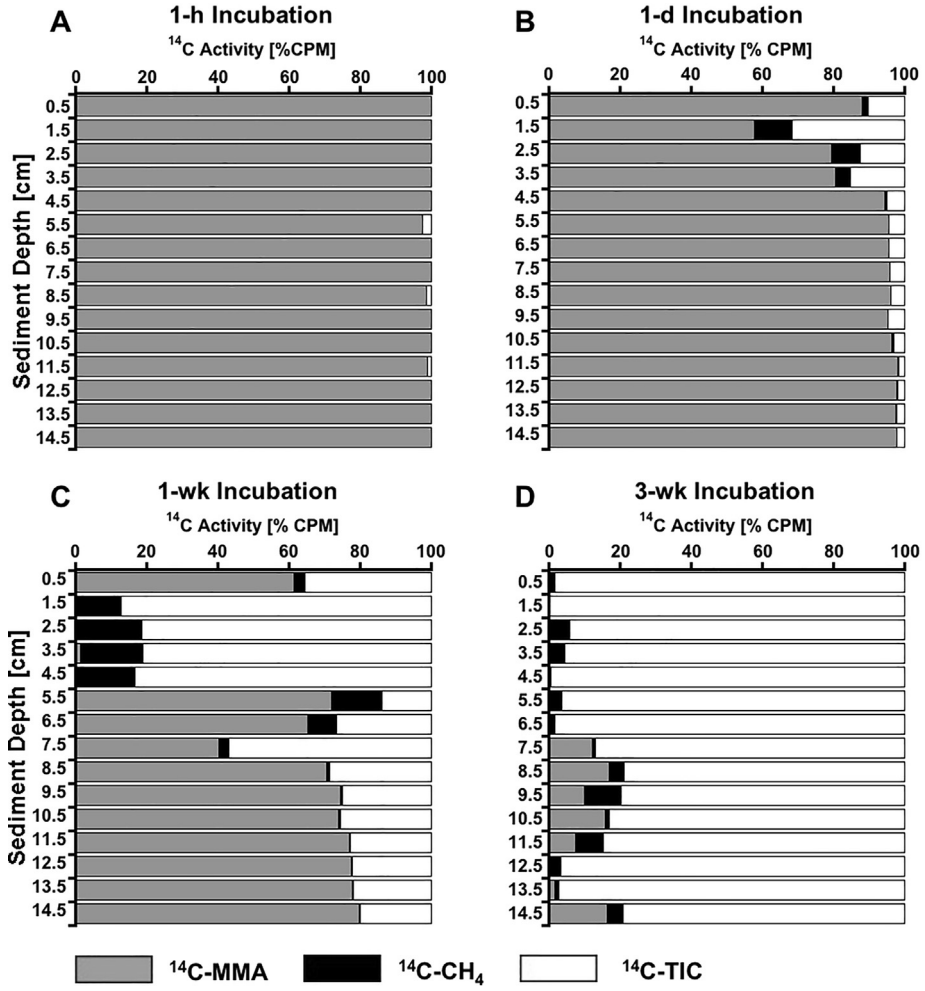

Fig. 5. Sediment depth profiles of ^{14}C radioactivity (in counts per minute = CPM) from mono-methylamine (MMA), CH_4, and total inorganic carbon (TIC) expressed as the percentage of the sum of all ^{14}C. Shown are depth profiles for 1-h (A), 1-d (B), 1-wk (C) and 3-wk (D) incubations in replicate sediment cores.

the core, while smaller percentages of radioactivity were found in ^{14}C-CH_4 (0–0.06%) and ^{14}C-TIC (1–5%) (Fig. 5A).

After the 1-d incubation, the percentage of ^{14}C-MMA was lower in the top 4 cm, reaching as low as 58% at 1–2 cm (Fig. 5B). Below 5 cm, 94–98% of the radioactivity remained in the ^{14}C-MMA. Correspondingly, more ^{14}C-CH_4 was detected in the top 5 cm, with a maximum of 11% at 0–2 cm. These depths of elevated ^{14}C-CH_4 overlapped with depths of elevated AOM-CH_4 and SR in replicate cores (Fig. 3). Below 5 cm, ^{14}C-CH_4 remained low (0.05–0.6%) (Fig. 5B). Similarly, the percentage of ^{14}C-TIC was higher (10–32%) in the top 5 cm with a maximum at 1–2 cm. Below 5 cm, the percentage of ^{14}C-TIC decreased gradually with depth from 5 to 2%.

After the 1-wk incubation, radioactivity from ^{14}C-MMA was below detection at 1–3 and 4–5 cm, pointing to complete exhaustion of the labeled compound (Fig. 5C). At depths below 5 cm, between 40 and 80% of the radioactivity remained in the ^{14}C-MMA. Radioactivity from ^{14}C-CH_4 was between 3 and 19% percent in the top 7 cm, with a maximum at 2–3 cm. Below 7 cm, 0.1–3% of radioactivity was found in ^{14}C-CH_4. Radioactivity from ^{14}C-TIC was 81 to 87% between 1–5 cm, indicating that the majority of the label was completely turned over. Below 7 cm, radioactivity from ^{14}C-TIC decreased from 57 to 20% with depth. It is notable that the production of ^{14}C-TIC was weaker at 5–6 and 6–7 cm (14 and 27%), while ^{14}C-CH_4 made up 14 and 8 % of the label, respectively.

After the 3-wk incubation, radioactivity from ^{14}C-MMA was below detection in the top 7 cm and at 12–13 cm (Fig. 5D). Between 7–12, and 13–15 cm, 2–17% of the radioactivity was found in the ^{14}C-MMA. Throughout the sediment core, a small fraction of radioactivity was detected in ^{14}C-CH_4 (0.05–10%), reaching a maximum at 9–10 cm. In the top 7 cm, most radioactivity was found in ^{14}C-TIC (94–99%). Below 7 cm, radioactivity of ^{14}C-TIC was more variable, ranging between 79–97%.

Note that radioactivity detected in the killed control samples was not subtracted from CPM results presented in Fig. 5, because we noticed after the analyses that microbial activity in the controls (and possibly also in the samples) was not immediately terminated after the addition of

NaOH, likely due to insufficient homogenization (shaking). Since killed controls were produced from the top 5 cm of the sediment, which also showed the highest microbial activity (see Fig. 5), it was not advisable to use the average of these controls to make CPM corrections for the entire sediment core. Radioactivity detected in the killed controls relative to the samples was on average 26%, 0.5%, 0.2%, and 0.3% for ^{14}C-CH_4, as well as 107%, 65%, 16%, and 9% for ^{14}C-TIC in the 1-h, 1-d, 1-wk, and 3-wk incubation, respectively. The development of ^{14}C-TIC in the controls relative to the samples indicates that microbial activity was likely terminated after roughly 1 day.

3.3.2. Estimation of environmental turnover rates

Fig. 6 compares MG-MMA rates with rates of AOM-MMA and AOM-CH_4. The MG-MMA rates were calculated assuming min/max concentrations of MMA (10 and 100 µM) based on a study by Fitzsimons et al. (1997) (for details see Section 2.5.4). AOM rate calculations were based on methane concentrations determined in the headspace of the incubation vials (Fig. 6B). We selected the 1-d incubation from the ^{14}C-MMA time series incubation as the optimum incubation time for rate calculations (see Section 4.3.1). Note that for these calculations, the average radioactivity detected in controls of the MMA incubation was subtracted from the sample values, which likely resulted in an underestimation of the rates, as microbial activity continued for ~1 d past incubation termination (see Section 2.5.4).

Activity of MG-MMA and AOM-MMA overlapped between 0–10 and 15–17 cm (Fig. 6). AOM-MMA rates were highest between 4–10 cm, peaking at 4–5 cm (27 nmol cm^{-3} d^{-1}), while MG-MMA rates were highest between 0–4 cm, peaking at 1–2 cm (3.3 and 33 nmol cm^{-3} d^{-1} for the 10 and 100 µM MMA, respectively). AOM-MMA was below detection between 10 and 15 cm, as a result of the control correction, while MG-MMA was low (<1 nmol cm^{-3} d^{-1}). AOM rates peaked between 15–17 cm (14 nmol cm^{-3} d^{-1}), while MG-MMA rates were low (0.1 and 1 nmol cm^{-3} d^{-1}, respectively).

In comparison, AOM-MMA and AOM-CH_4 reached similar maxima (10–30 nmol cm^{-3} d^{-1}), but slightly offset patterns in activity peaks (Fig. 6B). While AOM-MMA activity was separated between the top half and a lower section of the core, AOM-CH_4 showed three peaks: at 0–1 cm, between 7 and 12 cm, and at the bottom of the core.

Integrated rates (0–15 cm) of MG-MMA (based on 10/100 µM MMA), AOM-MMA, and AOM-CH_4 were 0.08/0.83, 1.74, and 0.88, respectively for the 1-d incubations.

4. DISCUSSION

4.1. Vertical organization of electron acceptor utilization

SR rates determined by ^{35}S-SO_4^{2-} incubations were highest in the top 1 cm layer of the sediment and restricted to the top 6 cm (Fig. 2C), illustrating a distinct sulfate-reducing environment. This finding is consistent with black coloration of the sediment in the top 1–8 cm, most likely due to precipitation of iron sulfides. Sulfate was never limiting (>63 mM) throughout the core, while salinity was found to be slightly higher (~15%) in the sulfate-reducing environment. Lack of direct water supply makes the pool highly susceptible to evaporation, which likely explains high salinity and sulfate concentrations. The abrupt drop of SR below 4 cm despite the presence of high sulfate concentrations is surprising and unlikely to be correlated to a limitation in organic matter, since coastal salt marshes are known to be rich in organic matter substrates in the top 50–100 cm (Schlesinger, 1977; Reddy and DeLaune, 2008; Ouyang and Lee, 2014). An explanation could be the stimulation of halophilic-sulfate reducers in the more saline surface layers of the sediment. A weak positive correlation between salinity and SR was found in natural sediments from hypersaline and highly saline coastal pans in South Africa (Porter et al., 2007; Oren, 2015). *In-vitro* sediment slurry experiments with these sediments revealed optimum salinities for sulfate-reduction activity was between 272 to 311 in hypersaline pans and 134 to 244 in highly saline pans.

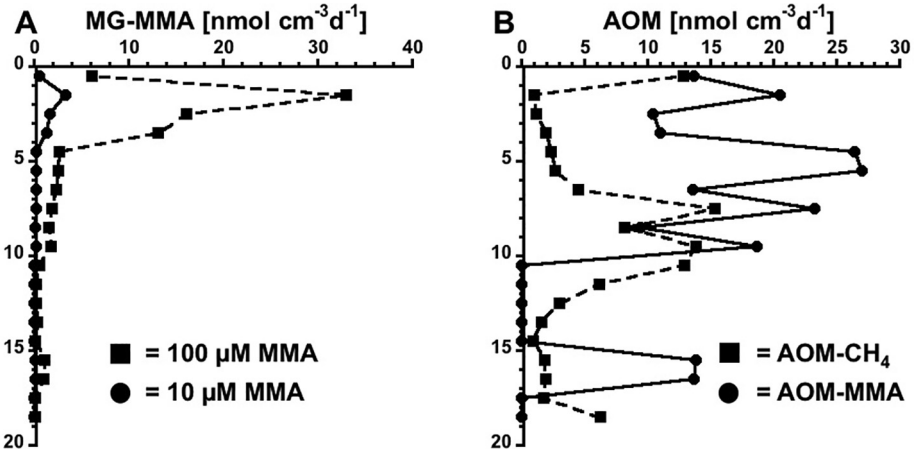

Fig. 6. Depth profiles of (A) methanogenesis rates determined from ^{14}C-MMA incubations (MG-MMA) assuming natural monomethylamine concentrations of 10 and 100 µM based on Fitzsimons et al. (1997), and (B) AOM rates determined from ^{14}C-CH_4 incubations (AOM-CH_4) and ^{14}C-MMA incubations (AOM-MMA) in hypersaline sediments from the Carpinteria Salt Marsh Reserve.

Below the zone of SR, the dominant electron acceptor for metabolic processes was likely iron (III), which is supported by the observation of brown spots (indicative for iron oxides, Fig. 1C) and the presence of dissolved iron (II) (Fig. 2D, product of iron reduction). Iron reduction activity could be an alternative reason for the absence of SR below 6 cm. In freshwater river sediments, SR was inhibited by 85–100% in the presences of iron reduction (Lovley and Phillips, 1987). However, direct evidence of iron reduction in the hypersaline pool is not available for this study and needs future investigation.

It is notable that both iron (II) and sulfide were present throughout the entire sediment core, i.e., sulfide was detected below the zone of SR and iron (II) was present within the sulfate-reducing zone. This finding points to potential seasonal fluctuations of processes in the sediment. It is possible that halophilic SR is only facilitated during the dry season, when salinity in the surface layer is highest, and is likewise inhibited during the wet season, when salinity drops below the salinity optimum. Consequently, our study would only provide a snapshot of a highly dynamic system. Future studies should therefore test if halophilic-sulfate reducers are outcompeting iron reducers during the dry season owing to their hypersaline adaptation.

The reverse redox gradient makes this hypersaline environment unique and unconventional compared to the usual succession of heterotrophic processes in marine sediments (Jørgensen, 2000), and possibly plays a role for cryptic methane cycling. Following suggested vertical distribution of redox processes, AOM activity determined by ^{14}C-CH_4 incubations was likely coupled to SR within the top 6 cm, and to iron reduction at depths below (Fig. 2B–D). This hypothesis is supported by double maxima of AOM at the surface (in alignment with the SR peak) and between 7 and 12 cm (in alignment with an increase in iron (II)). Both sulfate and iron (III) are known electron acceptors used by AOM (Nauhaus et al., 2002; Treude et al., 2005b; Beal et al., 2009; Segarra et al., 2013). It should be kept in mind, however, that aside from the availability of electron acceptors, also the distribution and magnitude of *in-situ* methane production plays an important role for the location of AOM hot spots in the sulfate-rich sediments.

4.2. Methanogenesis coupled to methylotrophic substrates

Considerable methane production was observed in sediment slurries, when either MMA or methanol was added (Fig. 4). Methanogenesis from MMA and methanol produced three orders of magnitude more methane than controls. The results suggest methylotrophic methanogens were present in the sediments and responded to the substrate addition. The spike in methane production after the 400 h (16 d) lag phase is likely a result of methanogen community expansion in response to excess availability of methylated substrates. This trend concurs with results of Oremland and Polcin (1982), who reported a spike in methane production in estuarian sediments after 10 d following the addition of trimethylamine, methanol and methyl-sulfides. Similarly, methanogenesis from methanol in sediments from Eckernförde Bay, SW Baltic Sea, observed a sharp methane increase after 16 d (Maltby et al., 2018).

Sediment slurries treated with molybdate showed a low increase in methane production in sediment from the 0–8 cm layer, which contained the sulfate-reducing zone, suggesting that methanogens were utilizing competitive substrates (acetate and/or hydrogen) following the inhibition of SR by molybdate (Oremland and Capone, 1988; Oremland and Taylor, 1978). Additionally, simultaneous inhibition of sulfate-dependent AOM likely suspended methane consumption. Methane in the bottom 8–16 cm layer showed no build-up over time after molybdate was added, suggesting that it had no inhibitory affect below the sulfate-reducing zone. This observation supports our hypothesis that organoclastic iron reduction dominated sediment below SR activity, because it is not affected by molybdate addition (Jacobson, 1994). Similarly, AOM coupled to iron reduction is not expected to be inhibited by molybdate addition and would therefore continue to consume methane in this zone.

The methanogen inhibitor BES suppressed methane production in both experiments, while controls showed a slight increase in methane over time, supporting the idea that methane was produced from in-situ methanogenic communities.

4.3. Deciphering cryptic methane cycling in sulfate-rich sediments

4.3.1. Method discussion

In this study, we conducted a radiotracer time series incubation with ^{14}C-MMA to determine the optimum incubation time for tracking the cryptic methane cycle. Short (~1 h) incubation times for radiotracer incubations have been found to cause issues with initial disturbance of the sediment, while long incubations (>1 d) can cause a gradual change in metabolism and chemical stratification of the sediment (Jørgensen, 1978). In the present study, we selected the 1-d (24-h) incubation as the optimal incubation period, because within this time frame sufficient products from both methanogenesis (^{14}C-CH_4) and AOM (^{14}C-TIC) were detected without considerably depleting the injected ^{14}C-MMA. Since this method depends on the production of an intermediate (^{14}C-CH_4) to track two processes in parallel, sufficient time should be provided for the intermediate to build up, while ensuring conditions in the sediment remain relatively stable. It should be kept in mind that the total incubation time was likely > 24 h due to the delay in incubation termination (see Section 3.3.1).

Tests of the radiotracer method demonstrated that each stage of the cryptic methane cycle (i.e., initial substrate: ^{14}C-MMA, intermediate substrate: ^{14}C-CH4, final product: ^{14}C-TIC) was successfully separated and quantified. Oven tests confirmed that only ^{14}C-CO_2 from combusted ^{14}C-CH4 was captured in the final trap. Similarly, the acidification/shaking tests confirmed that all ^{14}C-TIC was liberated as CO_2 and captured in the suspended CO_2 trap after shaking, while the ^{14}C-MMA remained in solution.

In Section 2.5.3 we showed that on average only 46% of ^{14}C-MMA initially injected into killed sediment from the

hypersaline pool was recovered in the sample supernatant. Methylamines are known to strongly adsorb to sediments through electrostatic and Van der Walls interactions (Wang and Lee, 1990, 1993; Fitzsimons et al., 2006; Zhuang et al., 2017, 2018). Applying a ^{14}C-MMA recovery factor of 0.46 to rate calculations (Eq. (7)) resulted in lower methanogenesis rates, because the factor is accounting for ^{14}C-MMA not captured by our standard analyses and hence increased the total pool of ^{14}C-MMA potentially available for methanogenesis. However, whether adsorbed ^{14}C-MMA is available for biological processes is currently unknown and needs additional studies. Future work should test the adsorption behavior of MMA with respect to different sediment types, because adsorption was reported to change with salinity, organic carbon, and clay mineral content (Wang and Lee, 1990, 1993; Xiao and Peacock, 2019). In our study, we recognized variability (22.5%) of ^{14}C-MMA recovery in replicate samples from different sediment depths, which indicates that differences in the absorption behavior might even occur within the same sediment core.

4.3.2. Methane cycling in the hypersaline sediments

The ^{14}C-MMA experiments demonstrated, for the first time, that carbon is directly shuttled from a methylotrophic substrate to CO_2 via CH_4, linking methanogenesis and AOM. Through increasing incubations times, we were able to show that radioactivity gradually shifted from MMA via CH_4 to TIC (Fig. 5A–D). Radioactive methane was detected in all four incubation experiments, confirming methanogenesis from MMA in the hypersaline sediments at the CSMR. Further, in all four incubations (from 1 h to 3 wk), the concentration of ^{14}C-CH_4 remained low. This observation matches with low natural methane concentrations found in the sediment (Fig. 2B) and with almost stationary concentration of methane in the headspace of natural control sediment in long-term incubations (Fig. 4F and L). Hence, the radiotracer method identified AOM as a powerful mechanism that keeps methane concentrations low within the sulfate-rich zone of the hypersaline sediment despite simultaneous methane production.

Determination of methylotrophic methanogenesis rates from the 1-d ^{14}C-MMA incubations, which assumed a natural MMA porewater concentration of 10 and 100 µM based on literature values (Fitzsimons et al., 1997), resulted in max rates of up to 3.3 and 33 nmol cm^{-3} d^{-1}, respectively, within the top 5 cm, i.e. within the sulfate-reducing zone (Fig. 6A). These maxima were 1–2 orders of magnitude higher compared to rates of total methanogenesis detected in the sulfate-reducing zone by Xiao et al. (2017. 2018), while rates in deeper zones of the sediment were in the same order of magnitude. The studies by Xiao et al. (2017. 2018) were conducted in sediments from Arhus Bay in the Baltic Sea, while our study was conducted in a hypersaline salt marsh. Salt marsh sediments are known for their richness in methylated substrates (Wang and Lee, 1994; Fitzsimons et al., 1997; Fitzsimons et al., 2005) and hence we believe that the estimated higher rates in our study are not unrealistic. However, determination of in-situ concentrations of MMA in sediments from the CSMR hypersaline pool are required to test this hypothesis.

AOM rates determined directly from ^{14}C-CH_4 and via ^{14}C-MMA injections (1 d incubation) ranged within the same order of magnitude (Fig. 6C). It should be kept in mind, however, that AOM rates determined from ^{14}C-MMA incubations likely underestimated the true AOM rate, since ^{14}C-CH_4 tracer was not added in one batch at t_0, but was instead produced from methanogenesis over time. Similarly, AOM rates determined from ^{14}C- CH_4 incubations could be underestimated, because the labeled methane was likely diluted by the production of new, unlabeled methane during the incubation. Irrespective of these uncertainties, confirmation of AOM activity by two separate methods suggests that AOM plays an important role in keeping methane concentrations in this sediment low.

It is notable that MMA could also be utilized by denitrifying bacteria (Martineau et al., 2015), and there is an ongoing debate about the potential involvement of sulfate reducers in the degradation of methylamines (Zhuang et al., 2019). However, to the best of our knowledge there is neither a confirmed case of denitrifying bacteria involved in MMA degradation in coastal wetland sediments, nor exists evidence for the metabolic capability of sulfate reducers to degrade MMA. Further work using methanogen and sulfate-reducer inhibitors in combination with ^{14}C-MMA incubations should be conducted to better elucidate the relationship between methylotrophic methanogens and sulfate-reducing bacteria in CSMR sediments.

4.4. Implications for methane budgeting in coastal wetlands

The present study demonstrated simultaneous production and consumption of methane in the sulfate-rich zone of a coastal wetland - a process that has to the best of our knowledge not been considered in previous coastal wetland studies. In combination, our results strongly indicate that methanogenesis was not able to build up significant concentrations of methane in the studied hypersaline sediments due to simultaneous activity of AOM. This finding could have important implications for our understanding of carbon cycling in coastal wetlands. While tremendous knowledge has been gained on methane production and emission from this type of environment (e.g., Oremland et al., 1982; Oremland and Polcin, 1982; Segers, 1998; Le Mer and Roger, 2001; Bridgham et al., 2013; Vizza et al., 2017), the underlying process that regulates emissions seems to be not fully understood. It is therefore necessary to consider cryptic methane cycling in coastal wetlands to predict potential future shifts in methane emission linked to the availability of electron acceptors for AOM. Environmental factors that could change electron acceptor availability in coastal wetland sediments include sea-level rise, droughts, increase in precipitation, and river run-offs, which are all likely to affect coastal wetlands in the near future (Junk et al., 2013; Mitsch et al., 2013; Mitsch and Hernandez, 2013; O'Connor et al., 2010).

5. CONCLUSION

In the present study, we investigated the relationship between SR, iron reduction, methylotrophic methanogene-

sis, and AOM in hypersaline sediment of the CSMR. Sediment slurry incubations with non-competitive substrates (MMA and methanol) indicated the presence of a methylotrophic methanogenic community. Our adapted radiotracer method successfully demonstrated that carbon is shuttled from MMA to TIC via CH_4, linking methanogenesis and AOM. The production and consumption of radioactive methane was detected both in the sulfate- and (apparently) iron-reducing zone of the sediment suggesting that (1) MMA served as a non-competitive substrate for methanogens and (2) AOM was coupled to both sulfate and iron reduction. Radioactive methane generated by methylotrophic methanogenesis remained always at a low level in ^{14}C incubations ranging from 1 h to 3 wk, suggesting that AOM was keeping up with the rate of methane production. Constant low levels of methane in the sediment despite the presence of methanogenesis identifies AOM as a potential key sink for methane produced in sulfate-rich sediment from this environment. The relationship between methanogenesis and AOM needs to be considered in future studies to complete carbon cycling in coastal wetlands and to evaluate the sensitivity of this balance to environmental changes.

6. RESEARCH DATA

Research Data associated with this article can be accessed at the Biological & Chemical Oceanography Data Management Office, DOI: https://doi.org/10.26008/1912/bco-dmo.839645.1.

Declaration of Competing Interest

The authors declare that they have no known competing financial interests or personal relationships that could have appeared to influence the work reported in this paper.

ACKNOWLEDGEMENTS

The authors thank the University of California Natural Reserve System and the Project Scientist of the Carpinteria Salt Marsh Reserve, A. Brooks, for authorizing the field sampling. We acknowledge J. Drake for providing fieldwork and laboratory instrument support. We also acknowledge K. Knight for her help with processing radioactive samples. We would like to thank G. Zhuang for his consultation of the development of the adapted combustion oven experimental setup. This work received financial support through the University of California and the National Science Foundation (NSF) (Award No.: 1852912).

REFERENCES

Beal E. J., House C. H. and Orphan V. J. (2009) Manganese- and iron-dependent marine methane oxidation. *Science* **325**, 184–187.

Boetius A., Ravenschlag K., Schubert C. J., Rickert D., Widdel F., Gieseke A., Amann R., Jørgensen B. B., Witte U. and Pfannkuche O. (2000) A marine microbial consortium apparently mediating anaerobic oxidation of methane. *Nature* **407**, 623–626.

Bridgham S. D., Megonigal J. P., Keller J. K., Bliss N. B. and Trettin C. (2006) The carbon balance of North American wetlands. *Wetlands* **26**(4), 889–916.

Bridgham S. D., Cadillo-Quiroz H., Keller J. K. and Zhuang Q. (2013) Methane emissions from wetlands: biogeochemical, microbial, and modeling perspectives from local to global scales. *Glob. Change Biol.* **19**, 1325–1346.

Cline J. D. (1969) Spectrophometric determination of hydrogen sulfide in natural waters. *Limnol. Oceanogr.* **14**, 454–458.

Dale A. W., Sommer S., Lomnitz U., Montes I., Treude T., Liebetrau V., Gier J., Hensen C., Dengler M., Stolpovsky K., Bryant L. D. and Wallmann K. (2015) Organic carbon production, mineralisation and preservation on the Peruvian margin. *Biogeosciences* **12**, 1537–1559.

Donnelly M. I. and Dagley S. (1980) Production of methanol from aromatic acids by Pseudomonas putida. *J. Bacteriol.* **142**(3), 916–924.

Fitzsimons M. F., Dawit M., Revitt D. M. and Rocha C. (2005) Effects of early tidal inundation on the cycling of methylamines in inter-tidal sediments. *Mar. Ecol. Prog. Ser.* **294**, 51–61.

Fitzsimons M. F., Jemmett A. W. and Wolff G. A. (1997) A preliminary study of the geochemistry of methylamines in a salt marsh. *Org Geochem.* **27**, 15–24.

Grasshoff K., Kremling K. and Ehrhardt M. (1999) Methods of Seawater Analysis. Wiley-VCH Verlag GmbH, Weinheim.

Hinrichs K.-U. and Boetius A. (2002) The anaerobic oxidation of methane: new insights in microbial ecology and biogeochemistry. In *Ocean Margin Systems* (eds. G. Wefer, D. Billett, D. Hebbeln, B. B. Jørgensen, M. Schlüter and T. Van Weering). Springer-Verlag, Berlin, pp. 457–477.

Hoehler T. M., Alperin M. J., Albert D. B. and Martens C. S. (1994) Field and laboratory studies of methane oxidation in an anoxic marine sediments: evidence for methanogen-sulphate reducer consortium. *Global Biochem. Cycles* **8**, 451–463.

IPCC (2007). The scientific basis. Contribution of Working Group I to the Fourth Assessment Report of the Intergovernmental Panel on Climate Change (IPCC). Cambridge University Press, Cambridge, MA.

IPCC, C.C. (2014). Mitigation of climate change. Contribution of working group III to the fifth assessment report of the intergovernmental panel on climate change.

Iversen N. and Jørgensen B. B. (1985) Anaerobic methane oxidation rates at the sulfate-methane transition in marine sediments from Kattegat and Skagerrak (Denmark). *Limnol. Oceanogr.* **30**(5), 944–955.

Jacobson M. (1994) Chemical and biological mobilization of Fe (III) in marsh sediments. *Biogeochemistry* **25**, 41–60.

Jørgensen B. B. and Kasten S. (2006) Sulfur cycling and methane oxidation. *Marine Geochemistry*. Springer, Berlin, Heidelberg, pp. 271–309.

Joye S. B., Boetius A., Orcutt B. N., Montoya J. P., Schulz H. N., Erickson M. J. and Logo S. K. (2004) The anaerobic oxidation of methane and sulfate reduction in sediments from Gulf of Mexico cold seeps. *Chem. Geol.* **205**, 219–238.

Junk W. J., An S., Finlayson C. M., Gopal B., Květ J., Mitchell S. A., Mitsch W. J. and Robarts R. D. (2013) Current state of knowledge regarding the world's wetlands and their future under global climate change: a synthesis. *Aquat. Sci.* **75**, 151–167.

Jørgensen B. B. (1978) A comparison of methods for the quantification of bacterial sulphate reduction in coastal marine sediments: I. Measurements with radiotracer techniques. *Geomicrobiol. J.* **1**, 11–27.

Jørgensen B. B. (2000) Bacteria and marine biogeochemistry. In *Marine Biogeochemistry* (eds. H. D. Schulz and M. Zabel). Springer Verlag, Berlin, pp. 173–201.

Kallmeyer J., Ferdelman T. G., Weber A., Fossing H. and Jørgensen B. B. (2004) A cold chromium distillation procedure for radiolabeled sulfide applied to sulfate reduction measurements. *Limnol. Oceanogr. Methods* **2**, 171–180.

Knittel K. and Boetius A. (2009) Anaerobic oxidation of methane: progress with an unknown process. *Annu. Rev. Microbiol.* **63**, 311–334.

Knudsen M. (1901) Hydrographical Tables According to the Measurings of Carl Forch...[et Al.] and with Assistance of Björn-Andersen...[et Al.]. *GEC Gad.*.

Krause, S. (2012) Effects of microbial activity on marine carbonates.

Kristjansson J. K., Schönheit P. and Thauer R. K. (1982) Different Ks values for hydrogen of methanogenic bacteria and sulfate reducing bacteria: an explanation for the apparent inhibition of methanogenesis by sulfate. *Arch. Microbiol.* **131**, 278–282.

Le Mer J. and Roger P. (2001) Production, oxidation, emission and consumption of methane by soils: a review. *Eur. J. Soil Biol.* **37**, 25–50.

Lovley D. R. and Klug M. J. (1986) Model for the distribution of sulfate reduction and methanogenesis in freshwater sediments. *Geochim. Cosmochim. Acta* **50**, 11–18.

Lovley D. R. and Phillips E. J. (1987) Competitive mechanisms for inhibition of sulfate reduction and methane production in the zone of ferric iron reduction in sediments. *Appl. Environ. Microbiol.* **53**, 2636–2641.

Maltby J., Sommer S., Dale A. W. and Treude T. (2016) Microbial methanogenesis in the sulfate-reducing zone of surface sediments traversing the Peruvian margin. *Biogeosciences* **13**, 283–299.

Maltby J., Steinle L., Loscher C., Bange H., Fischer M., Schmidt M. and Treude T. (2018) Microbial methanogenesis in the sulfate-reducing zone of sediments in the Eckernforde Bay, SW Baltic Sea. *Biogeosciences* **15**, 137–157.

Martineau C., Mauffrey F. and Villemur R. (2015) Comparative analysis of denitrifying activities of Hyphomicrobium nitrativorans, Hyphomicrobium denitrificans, and Hyphomicrobium zavarzinii. *Appl. Environ. Microbiol.* **81**, 5003–5014.

Michaelis W., Seifert R., Nauhaus K., Treude T., Thiel V., Blumenberg M., Knittel K., Gieseke A., Peterknecht K., Pape T., Boetius A., Aman A., Jørgensen B. B., Widdel F., Peckmann J., Pimenov N. V. and Gulin M. (2002) Microbial reefs in the Black Sea fueled by anaerobic oxidation of methane. *Science* **297**, 1013–1015.

Mitsch W. J., Bernal B., Nahlik A. M., Mander Ü., Zhang L. i., Anderson C. J., Jørgensen S. E. and Brix H. (2013) Wetlands, carbon, and climate change. *Landscape Ecol.* **28**, 583–597.

Mitsch W. J. and Hernandez M. E. (2013) Landscape and climate change threats to wetlands of North and Central America. *Aquat. Sci.* **75**, 133–149.

Nauhaus K., Boetius A., Krüger M. and Widdel F. (2002) In vitro demonstration of anaerobic oxidation of methane coupled to sulphate reduction in sediment from marine gas hydrate area. *Environ. Microbiol.* **4**, 298–305.

Nisbet E. G., Manning M., Dlugokencky E., Fisher R., Lowry D., Michel S., Myhre C. L., Platt S. M., Allen G. and Bousquet P. (2019) Very strong atmospheric methane growth in the 4 years 2014–2017: Implications for the Paris Agreement. *Global Biogeochem. Cycles* **33**, 318–342.

O'Connor F. M., Boucher O., Gedney N., Jones C. D., Folberth G. A., Coppell R., Friedlingstein P., Collins W. J., Chappellaz J., Ridley J. and Johnson C. E. (2010) Possible role of wetlands, permafrost, and methane hydrates in the methane cycle under future climate change: a review. *Rev. Geophys.* **48**. https://doi.org/10.1029/2010RG000326.

Oremland R. S. and Capone D. G. (1988) Use of specific inhibitors in biogeochemistry and microbial ecology. In *Advances in Microbial Ecology* (ed. K. C. Marshall). Pleneum Press, New York, pp. 285–383.

Oremland R. S., Marsh L. M. and Polcin S. (1982) Methane production and simultaneous sulphate reduction in anoxic, salt marsh sediments. *Nature* **296**, 143–145.

Oremland R. S. and Polcin S. (1982) Methanogenesis and sulfate reduction: competitive and noncompetitive substrates in estuarine sediments. *Appl. Environ. Microbiol.* **44**, 1270–1276.

Oremland R. S. and Taylor B. F. (1978) Sulfate reduction and methanogenesis in marine sediments. *Geochim. Cosmochim. Acta* **42**, 209–214.

Oren A. (1990) Formation and breakdown of glycine betaine and trimethylamine in hypersaline environments. *Antonie Van Leeuwenhoek* **58**, 291–298.

Oren A. (2015) Halophilic microbial communities and their environments. *Curr. Opin. Biotechnol.* **33**, 119–124.

Orphan V. J., House C. H., Hinrichs K.-U., McKeegan K. D. and De Long E. F. (2001) Methane-consuming Archaea revealed by directly coupled isotopic and phylogenetic analysis. *Science* **293**, 484–487.

Ouyang X. and Lee S. Y. (2014) Updated estimates of carbon accumulation rates in coastal marsh sediments. *Biogeosciences* **11**, 5057–5071.

Page H. M., Petty R. L. and Meade D. E. (1995) Influence of watershed runoff on nutrient dynamics in a southern California salt marsh. *Estuar. Coast. Shelf Sci.* **41**, 163–180.

Porter D., Roychoudhury A. N. and Cowan D. (2007) Dissimilatory sulfate reduction in hypersaline coastal pans: activity across a salinity gradient. *Geochim. Cosmochim. Acta* **71**, 5102–5116.

Reddy K. R. and DeLaune R. D. (2008) *Biogeochemistry of Wetlands*. CRC Press, Taylor & Francis Group, Boca Raton.

Reeburgh W. S. (2007) Oceanic methane biogeochemistry. *Chem. Rev.* **107**, 486–513.

Saunois M., Stavert A. R., Poulter B., Bousquet P., Canadell J. G., Jackson R. B., Raymond P. A., Dlugokencky E. J., Houweling S. and Patra P. K. (2020) The global methane budget 2000–2017. *Earth Syst. Sci. Data* **12**, 1561–1623.

Schink B. and Zeikus J. G. (1980) Microbial methanol formation: a major end product of pectin metabolism. *Curr. Microbiol.* **4**(6), 387–389.

Schlesinger W. H. (1977) Carbon balance in terrestrial detritus. *Annu. Rev. Ecol. Syst.* **8**, 51–81.

Segarra K. E. A., Comerford C., Slaughter J. and Joye S. B. (2013) Impact of electron acceptor availability on the anaerobic oxidation of methane in coastal freshwater and brackish wetland sediments. *Geochim. Cosmochim. Acta* **115**, 15–30.

Segers R. (1998) Methane production and methane consumption: a review of processes underlying wetland methane fluxes. *Biogeochemistry* **41**, 23–51.

Stephenson M. and Stickland L. H. (1933) CCVII. Hydrogenase. III. The bacterial formation of methane by the reduction of one-carbon compounds by molecular hydrogen. *Biochem. J.* **27**, 1517–1527.

Thauer R. K. (1998) Biochemistry of methanogenesis: a tribute to Marjory Stephenson. *Microbiology* **144**, 2377–2406.

Treude T., Krüger M., Boetius A. and Jørgensen B. B. (2005a) Environmental control on anaerobic oxidation of methane in the gassy sediments of Eckernförde Bay (German Baltic). *Limnol. Oceanogr.* **50**, 1771–1786.

Treude T., Niggemann J., Kallmeyer J., Wintersteller P., Schubert C. J., Boetius A. and Jørgensen B. B. (2005b) Anaerobic

oxidation of methane in the sulfate-methane transition along the Chilean continental margin. *Geochim. Cosmochim. Acta* **69**, 2767–2779.

Vizza C., West W. E., Jones S. E., Hart J. A. and Lamberti G. A. (2017) Regulators of coastal wetland methane production and responses to simulated global change. *Biogeosciences* **14**(2), 431–446.

Wang X.-C. and Lee C. (1990) The distribution and adsorption behavior of aliphatic amines in marine and lacustrine sediments. *Geochim. Cosmochim. Acta* **54**, 2759–2774.

Wang X.-C. and Lee C. (1993) Adsorption and desorption of aliphatic amines, amino acids and acetate by clay minerals and marine sediments. *Mar. Chem.* **44**, 1–23.

Wang X.-C. and Lee C. (1994) Sources and distribution of aliphatic amines in salt marsh sediment. *Org. Geochem.* **22**, 1005–1021.

Widdel F. and Bak F. (1992) Gram-negative mesophilic sulfate-reducing bacteria. In *The Prokaryotes* (eds. A. Balows, H. G. Trüper, M. Dworking, W. Harder and K. H. Schleifer). Springer, New York, pp. 3352–3378.

Winfrey M. R. and Ward D. M. (1983) Substrates for sulfate reduction and methane p roduction in i ntertidal sediments. *Appl. Environm. Microbiol* **45**, 193–199.

Xiao K., Beulig F., Kjeldsen K., Jorgensen B. and Risgaard-Petersen N. (2017) Concurrent methane production and oxidation in surface sediment from Aarhus Bay, Denmark. *Front. Microbiol.* **8**.

Xiao K.-Q. and Peacock C. (2019) The Role of Minerals in Cryptic Methane Cycling in Marine Surface Sediment.

Xiao K. Q., Beulig F., Røy H., Jørgensen B. B. and Risgaard-Petersen N. (2018) Methylotrophic methanogenesis fuels cryptic methane cycling in marine surface sediment. *Limnol. Oceanogr.* **63**, 1519–1527.

Zhuang G.-C., Elling F. J., Nigro L. M., Samarkin V., Joye S. B., Teske A. and Hinrichs K.-U. (2016) Multiple evidence for methylotrophic methanogenesis as the dominant methanogenic pathway in hypersaline sediments from the Orca Basin, Gulf of Mexico. *Geochim. Cosmochim. Acta* **187**, 1–20.

Zhuang G.-C., Heuer V. B., Lazar C. S., Goldhammer T., Wendt J., Samarkin V. A., Elvert M., Teske A. P., Joye S. B. and Hinrichs K.-U. (2018) Relative importance of methylotrophic methanogenesis in sediments of the Western Mediterranean Sea. *Geochim. Cosmochim. Acta* **224**, 171–186.

Zhuang G.-C., Lin Y.-S., Bowles M. W., Heuer V. B., Lever M. A., Elvert M. and Hinrichs K.-U. (2017) Distribution and isotopic composition of trimethylamine, dimethylsulfide and dimethylsulfoniopropionate in marine sediments. *Mar. Chem.* **196**, 35–46.

Zhuang G.-C., Montgomery A. and Joye S. B. (2019) Heterotrophic metabolism of C1 and C2 low molecular weight compounds in northern Gulf of Mexico sediments: controlling factors and implications for organic carbon degradation. *Geochim. Cosmochim. Acta* **247**, 243–260.

Zhuang G.-C., Yang G., Yu J. and Gao Y. (2011) Production of DMS and DMSP in different physiological stages and salinity conditions in two marine algae. *Chinese J. Oceanol. Limnol.* **29**, 369–377.

Associate editor: Edward Hornibrook